

## Earthshine and the Earth's albedo:

### 2. Observations and simulations over 3 years

E. Pallé,<sup>1</sup> P. R. Goode,<sup>1,2</sup> V. Yurchyshyn,<sup>1</sup> J. Qiu,<sup>1</sup> J. Hickey,<sup>1</sup> P. Montañés Rodríguez,<sup>1</sup> M.-C. Chu,<sup>3</sup> E. Kolbe,<sup>4</sup> C. T. Brown,<sup>5</sup> and S. E. Koonin<sup>5</sup>

Received 19 March 2003; revised 12 August 2003; accepted 26 August 2003; published 29 November 2003.

[1] Since late 1998, we have been making sustained measurements of the Earth's reflectance by observing the earthshine from Big Bear Solar Observatory. Further, we have simulated the Earth's reflectance for both the parts of the Earth in the earthshine and for the whole Earth. The simulations employ scene models of the Earth from the Earth Radiation Budget Experiment, simulated snow/ice cover, and near-real-time satellite cloud cover data. Broadly, the simulations and observations agree; however, there are important and significant differences, with the simulations showing more muted variations. During the rising phase of the Moon we measure the sunlit world to the west of California, and during the declining lunar phase we measure the sunlit world to the east. Somewhat surprisingly, the one third of the Earth to the west and that to the east have very similar reflectances, in spite of the fact that the topographies look quite different. The part to the west shows less stability, presumably because of the greater variability in the Asian cloud cover. We find that our precision, with steady observations since December 1998, is sufficient to detect a seasonal cycle. We have also determined the annual mean albedos both from our observations and from simulations. To determine a global albedo, we integrate over all lunar phases. Various methods are developed to perform this integration, and all give similar results. Despite sizable variation in the reflectance from night to night and from season to season (which arises from changing cloud cover), we use the earthshine to determine annual albedos to better than 1%. As such, these measurements are significant for measuring climate variation and are complementary to satellite determinations.

*INDEX TERMS:* 0320 Atmospheric Composition and Structure: Cloud physics and chemistry; 0325 Atmospheric Composition and Structure: Evolution of the atmosphere; 1610 Global Change: Atmosphere (0315, 0325); 3354 Meteorology and Atmospheric Dynamics: Precipitation (1854); 7536 Solar Physics, Astrophysics, and Astronomy: Solar activity cycle (2162); *KEYWORDS:* albedo, Earth, Moon

**Citation:** Pallé, E., P. R. Goode, V. Yurchyshyn, J. Qiu, J. Hickey, P. Montañés Rodríguez, M.-C. Chu, E. Kolbe, C. T. Brown, and S. E. Koonin, Earthshine and the Earth's albedo: 2. Observations and simulations over 3 years, *J. Geophys. Res.*, 108(D22), 4710, doi:10.1029/2003JD003611, 2003.

### 1. Introduction

[2] In Qiu *et al.* [2003] (hereinafter referred to as Paper 1), we have detailed our method of determining the Earth's reflectance from photometric observations of the bright (moonshine) and dark (earthshine) parts of the lunar disk. We have demonstrated that we can measure the large-scale apparent albedo of the Earth to a precision of about 1% on any

given night. Here we discuss the results of more than 3 years of observations of the earthshine. In addition, we have simulated the reflectance of the Earth, treating separately the parts in the earthshine and all the sunlit Earth throughout the hours of the day. In the simulations, we use scene models of the Earth from the Earth Radiation Budget Experiment (ERBE) and near-real-time satellite cloud cover data. We discuss and compare the observational results with those of the simulations.

[3] On any single night, we determine the reflectance of most of the sunlit Earth for a particular phase of the Moon (the apparent albedo). As detailed in Paper 1, we need to integrate over all phases of the Moon to determine a global or Bond albedo for the Earth:

$$A = \frac{2}{3} \int_{-\pi}^{\pi} d\theta p^*(\theta) f_L(\theta) \sin \theta, \quad (1)$$

where  $p^*$  is the apparent albedo associated with a particular night,  $f_L(\theta)$  is the Moon's Lambert phase function and  $A$  is the Bond albedo.

<sup>1</sup>Big Bear Solar Observatory, New Jersey Institute of Technology, Newark, New Jersey, USA.

<sup>2</sup>Also at W. K. Kellogg Radiation Laboratory, California Institute of Technology, Pasadena, California, USA.

<sup>3</sup>Department of Physics, The Chinese University of Hong Kong, Hong Kong, China.

<sup>4</sup>Department für Physik and Astronomie, Universität Basel, Basel, Switzerland.

<sup>5</sup>W. K. Kellogg Radiation Laboratory, California Institute of Technology, Pasadena, California, USA.

[4] The apparent albedo is the albedo of a Lambert sphere that would give the same instantaneous reflectivity as the true Earth at the same phase angle, and where an unchanged  $p^*$  as a function of phase angle would imply a Lambertian Earth (see Paper 1 for a more detailed discussion of  $p^*$ ). The apparent albedo value for an individual night is calculated from the earthshine measurements for that night using

$$p^*(\beta) = \frac{3}{2f_L} \frac{p_b f_b(\theta)}{p_a f_a(\theta_0)} \frac{I_a/T_a}{I_b/T_b} \frac{R_{EM}^2 R_{ES}^2}{R_E^2 R_{MS}^2}, \quad (2)$$

where  $\beta$  is the Earth's phase angle (the angle between the sunlight that is incident somewhere on the Earth and reflected, as earthshine, to the Moon),  $(I_a/T_a)/(I_b/T_b)$  is the ratio of the earthshine intensity to the moonshine intensity in two opposing fiducial patches, after each is corrected for air mass, and  $p_b/p_a$  is the ratio between the geometrical reflectivity of the two opposing fiducial patches.  $R_{EM}$ ,  $R_{ES}$ ,  $R_{MS}$  and  $R_E$  refer to the Earth-Moon distance, the Earth-Sun distance, the Moon-Sun distance and the Earth's radius respectively. The lunar phase function for the bright side,  $f_b(\theta)$ , is used in the formula to account for the geometrical dependence of the reflectivity of the Moon, while  $f_a(\theta_0)$  accounts for the fact that the earthshine is not exactly retroreflected from the Moon ( $\theta_0 \lesssim 1^\circ$ ).

[5] For convenience, the measured Earth's albedo is often expressed as the magnitude of the apparent albedo,  $p^*$ , i.e.,

$$m(p^*) = -2.5 \log p^*. \quad (3)$$

This standard astronomical definition implies that the larger  $m(p^*)$  is the smaller the albedo. Note that a 1% change in  $p^*$  corresponds to about  $0^m.01$  change in  $m(p^*)$ .

[6] Each night, we observe 10 fiducial patches, five on the Crisium side, and five on the Grimaldi side (see Figure 3 in Paper 1). In principle, we obtain 25 values of  $p^*$  from the 25 combinations of the five pairs of fiducial patches. This gives us a way to evaluate the reliability of our measurement of  $p^*$  as detailed in section 5. Figures 12a and 12b show the  $p^*$  plot, morning (Moon's phase angle decreasing toward new) and evening (Moon's phase angle increasing toward full), against lunar phase angle for the mean of the 25 data sets for each night. It is clear that the same pattern of variation appears in all data sets, indicating that this pattern is real, and not from measurement noise. We take an average of the 25 measurements of  $m(p^*)$  for each night as shown in Figure 12c, and the standard deviation of the mean in  $m(p^*)$  is calculated as 0.016 and 0.018 for morning and evening respectively, yielding a measurement accuracy of sigma better than 2%. In detail, we calculated the  $\sigma^2 = [\sum_i (m(p^*)_i - \overline{m(p^*)})^2] / (N - 1)$ , where  $N = 25$  and  $1 \leq i \leq 25$ .

[7] So far, observational data have been accumulated for more than 40 months covering the winter of 1998–1999 through the early 2002 (9 December 1998 to 31 March 2002). Both the instantaneous  $m(p^*)$  variation during each single night, and the Bond albedo integrations over a long period of time, have been obtained and compared to the

simulated results using a scene model, snow/ice cover data and satellite cloud cover data.

## 2. Modeling the Observations

[8] In principle, we have sufficient information to determine a Bond albedo from the simulations by using scene models of the Earth, and adding cloud cover data from satellites and snow/ice cover from models. However, a precise determination is no easy matter. In particular, the treatment of the clouds is probably a bit oversimplified, and we ignore any other climate parameters, beyond snow and ice, that might contribute to changes in albedo. Further, the ERBE model contemplates only 12 different scenes and four cloudiness levels (0–5%, 5–50%, 50–95%, and 95–100%). Beyond the appreciable binning of the cloud cover, changes in cloud type or cloud optical thickness, for example, will also affect the albedo, but these are not accounted for in the models. Thus our albedo models presented here need to be considered only as a first-order, or starting, approximation to the problem.

[9] In general, the Bond albedo is given in terms of the albedo of each element of the Earth's surface by

$$A = \frac{1}{\pi R_E^2} \int d^2R (\hat{R} \cdot \hat{S}) a, \quad (4)$$

where  $d^2R$  is an element of the Earth's surface,  $\hat{R}$  is a unit vector pointing toward the local zenith, and  $\hat{S}$  is a unit vector pointing toward the Sun. The albedo of each surface element,  $a$ , depends on the surface type, cloud and snow/ice cover and solar zenith angle. Further, there is an anisotropic factor that gives the angular distribution of the reflected radiation and depends upon the reflected zenith angle and azimuth. The integral is over all portions of the globe illuminated by the Sun (i.e.,  $(\hat{R} \cdot \hat{S}) \geq 0$ ). However, to compare the simulations with our observations, we have to consider the ratio of the earthlight to sunlight,  $\Gamma$ , that would be seen by an observer on the Moon.

[10] There is a systematic variation of  $\Gamma$  throughout the lunar month. When the Moon is nearly new (lunar phase  $\theta \approx \pm\pi$ ), the Earth is nearly full, and so  $\Gamma$  is relatively large ( $\approx 10^{-4}$ ). Conversely, when the Moon is nearly full ( $\theta \approx 0$ ), the Earth is a thin crescent and  $\Gamma$  becomes vanishingly small. Fluctuations of  $\Gamma$  about its systematic behavior are caused by varying terrestrial conditions, including weather, the seasons and climate change. The lunar phase  $\theta$  is defined in Figure 2 of Paper 1. After correction for the dependence of the reflectivity on lunar phase, one obtains

$$\Gamma = \frac{1}{\pi R_{EM}^2} \left[ \frac{R_{MS}}{R_{ES}} \right]^2 \int_{(\hat{R} \cdot \hat{S}, \hat{R} \cdot \hat{M}) \geq 0} d^2R (\hat{R} \cdot \hat{S}) a(\hat{R} \cdot \hat{M}) L, \quad (5)$$

where  $\hat{M}$  is the unit vector pointing from the Earth toward the Moon, and the integral is over all of the Earth's surface for which the Sun and Moon are simultaneously above the horizon (i.e.,  $\hat{R} \cdot \hat{S}$  and  $\hat{R} \cdot \hat{M} \geq 0$ ). The anisotropy function,  $L$ , generally depends on surface type, cloud cover, and the zenith angles and relative azimuth of the Sun and Moon.  $L$  is defined so that it is unity for a Lambert surface (see equation (8) in Paper 1). The apparent albedo,  $p^*$ , of the

partly sunlit Earth disk observed by way of the Moon can be related to the normalized bidirectional reflectance factor  $R = \pi \frac{N}{M}$  used in Earth radiation budget studies from satellite data, where  $N$  is the reflected radiance observed in a particular direction from a small region and  $M$  is the reflected flux through a horizontal surface in that same region, so that the earthshine-derived  $p^*$  is a sort of weighted average of  $R$ . In terms of equation (10) of Paper 1,

$$p^* = \frac{3}{2f_L} \Gamma \frac{R_{EM}^2 R_{ES}^2}{R_E^2 R_{MS}^2} \quad (6)$$

because  $\Gamma$  is the ratio of the earthshine to moonshine intensity that would be seen by an observer on Earth looking at the Moon, there is no dependence on lunar reflectivity.

[11] Thus our models enable us to simulate for a given night (or a subset of time during 1 night) the Bond albedo of the Earth, and the apparent albedo that would be seen from BBSO.

[12] In modeling the reflectance properties,  $a$  and  $L$ , of the Earth, we used scene models developed for the ERBE observations [Suttles *et al.*, 1988]. The model reflectances are defined as a mean over the broad shortwave interval from 200 to 4000 nm, while our observations cover the spectral range from 400 to 700 nm. As mentioned,  $a$  and  $L$  are tabulated for 12 model scenes, varying from “desert” (areas for which the annual precipitation is less than 26 cm) to “mixed land-ocean” areas, which are cells bordered by two land and two ocean cells. For the snow/ice cover, we used simulations from the Canadian Center for Climate Modeling and Analysis (CCCM II; <http://www.cccma.bc.ec.gc.ca>). This Gaussian grid spacing is roughly  $2.8^\circ \times 2.8^\circ$  in longitude and latitude. The model gives the monthly mean snow/ice cover for each grid cell. The simulations of the Earth’s albedo were performed using two different cloud cover data sets.

[13] Our primary data set for the model calculations is uncalibrated images of the global cloud cover produced by the Weather Services International (WSI) Corporation. We use these data in the simulations of our observations. The WSI Corporation is the only place we know of that is currently producing near-real-time, on-line publication of global cloud cover maps. WSI maps (<http://www.intellicast.com>) are composed of data from both geostationary and polar orbiting satellites. Data from multiple orbits are mosaicked together to provide wide-scale global and full Earth views in a single image. To allow for continuous night and day viewing of cloud patterns, infrared imagery is used. We download and calibrate daily WSI images.

[14] We have also used the daily (D2) and monthly (D2) mean fractional cloud cover data from International Satellite Cloud Climatology Project (ISCCP). The presently released ISCCP data set covers 18 years over the period July 1983 through September 2001. The ISCCP data set makes use of visible and infrared radiances; total cloudiness is determined using both of them, whereas the various cloud types are determined using infrared radiances only. For further details on the ISCCP data, see Rossow *et al.* [1996]. All ISCCP data products are archived at the ISCCP Central Archive (<http://isccp.giss.nasa.gov>).

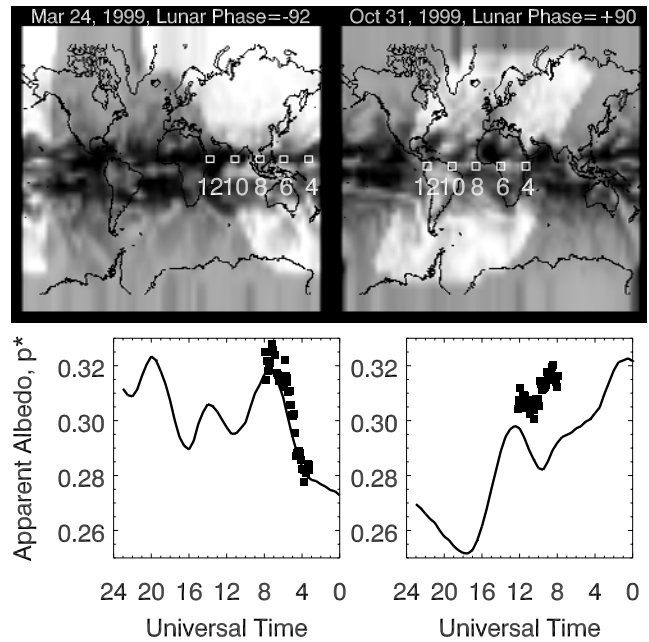


**Figure 1.** (top) Extended bright areas highlighting those parts of the Earth that are the source of the earthshine. The satellite-derived WSI cloud cover maps are shown in a secondary gray scale, with brighter areas indicating greater cloud cover. For 31 October 1999, note that the northernmost regions are not sunlit, and the southernmost regions do not contribute to earthshine because the Moon is fairly far north in the sky. The empty white boxes indicate the longitudes of maximal contribution to the earthshine at the UT shown. (bottom) Solid boxes show the observed apparent albedo as a function of time (note that the time axis is reversed), while the solid line indicates the simulated  $p^*$  values for the night.

[15] Whereas ISCCP cloud data is given in percentage cloud coverage, the WSI images we download from the web are given in arbitrary units, and it is necessary to translate them into fractional coverage. The daily WSI images are each placed on a “T42” square grid ( $2.8^\circ \times 2.8^\circ$ ), as are the ISCCP data. We make use of the “T42” square grid because this is the format for snow and ice data, albeit one of the most common formats for climatological data. We have made WSI monthly mean cloud cover maps (values are in arbitrary units), and compared them with the ISCCP monthly mean maps (in units of fractional cloud cover). Primarily, we are looking for completely overcast areas. We find those areas with the minimum number of counts in the WSI images, and assign 100% cloud cover for any number of counts equal or greater to this minima. We also look for clear sky scenes and we assign a maximum number of counts in WSI images below which we consider them to be 0% cloud cover. The values between the maxima and minima are converted to percentage coverage units using a simple polynomial parameterization. This yields an empirical nonlinear calibration curve between the two cloud data sets, by which WSI daily maps in arbitrary units are converted into ISCCP fractional coverage, although this does not translate into a one-to-one correspondence between the two data sets. Important differences between the two

still occur. The use of a different calibration curve can altogether increase or decrease the mean albedo, but cannot increase the muted seasonal variations derived from the models.

### 3. Comparing Daily Observations and Model Results

[16] In Figure 1, we show evening and morning earthshine observations overlaid on model calculations covering the entire day. Figure 1 (bottom) shows the earthshine as a function of time. The solid curve shows the variation of the calculated apparent albedo  $p^*$  during the 24-hour period, and the solid boxes are the observed apparent albedo. These results come from near to a quarter Moon, and are compared with the Earth-wide WSI cloud cover from the same day in Figure 1 (top).

[17] Figure 1 (top) shows the cloud cover maps illustrating which parts of the Earth contributes to the earthshine. We highlight (the large bright areas) those parts of the Earth that are the source of the earthshine (i.e., are simultaneously in the sunshine and are visible from the Moon at some time during the observations). The cloud cover is also shown as secondary gray scale, for instance, the east-west dark bands just north and south of the equator illustrate cloudless areas. We also indicate with boxes an intersection of the Earth's surface with the bisectrix of the spatial angle between the surface intersection of the lines from the center of the Earth to the Moon and the Sun or, in other words, the point of equal angles, where the angle of incidence is equal to the angle of reflection.

[18] The observations are consistent with the simulations for 24 March 1999, which is one of the nights for which the agreement is quite good. On 31 October 1999, a more typical night, there is a discrepancy of about 5% relative (or 0.015 absolute) in the apparent albedo. One may notice offsets between the simulations and observations in Figure 1 (bottom), but must bear in mind that the cloud cover data are a composite of many observations that are taken over about 6 hours (and sometimes up to 24). Thus a precise timing between the observations and simulations is not possible. We simply assume that the cloud cover is invariant from one posting to the next and we make no effort to smooth the transition. If there were a rapid cloud formation or movement, it could result in observational and simulated results which do not have the same form. However, this does not account for the apparent offset in the albedo.

[19] At high geographical latitudes above  $45^\circ$ , the cloud cover is fairly steady. Thus the short timescale variations in reflectance in Figure 1 are due primarily to irregularities in the fractional cloud cover at low latitudes, and secondarily to the scene type. In the lower left panel of Figure 1, one sees that the observed and calculated maxima in  $p^*$  at 0700 UT are due to a relative cloud excess over the Far East, while the calculated local minimum in  $p^*$  at 1100 UT arises from the cloudless area above India and the Arabian Sea. In the lower left panel of Figure 1, there is a more than a 10% change in  $p^*$  over about 2 hours. This sharp increase is due to the increasing contribution of a cloudy Asia to the Earth's reflectance as the Earth rotates. An offset between the observed and calculated apparent

albedos is evident in the lower right panel of Figure 1. Typically, the observed results vary more about the mean than do the simulated ones.

### 4. Seasonal Changes in Apparent Albedo, $p^*$

[20] We have nearly 400 nights of observations covering the period from December 1998 to January 2003. For each of these nights, a mean apparent albedo,  $p^*$ , is measured. Here we use observations and simulations to probe the Earth's albedo by determining its seasonal variability (or anomalies). The seasonal variation of the Earth's reflectance is not well known. In fact, *Goode et al.* [2001] have shown that over a year and a half (1999.0–2000.5), the Earth's seasonal variation is more than 10%. This surprisingly large value was twice that determined from the simulations covering the same nights and the same parts of the Earth.

[21] To determine seasonal anomalies, a fit to the lunar phase dependence of  $p^*$  is calculated for all the available data. Then, for each night the difference between the  $p^*$  for that night (and lunar phase) and the mean value given by the fit to all nights is determined; this constitutes the anomaly for that night.

[22] Starting from equation (2), the fractional seasonal variation depends only on the observed intensities corrected for air mass; that is,

$$\sum_{i=1}^N \frac{p_{\text{seas}}^*(\theta_i) - \overline{p^*}(\theta_i)}{\overline{p^*}(\theta_i)} = \sum_{i=1}^N \frac{\left( \frac{I_a/T_a R_{EM}^2 R_{ES}^2}{I_b/T_b R_{MS}^2} \right)_{\text{seas},i} - \left( \frac{I_a/T_a R_{EM}^2 R_{ES}^2}{I_b/T_b R_{MS}^2} \right)_i}{\left( \frac{I_a/T_a R_{EM}^2 R_{ES}^2}{I_b/T_b R_{MS}^2} \right)_i}, \quad (7)$$

where  $N$  is the number of nights for which we have data in a particular season,  $\theta_i$  is the lunar phase on the  $i$ th night of that season, and  $\overline{p^*}(\theta_i)$  is the fit shown in Figure 13 (section 6). The average for a particular season is computed from each night's data by determining the fractional change for that night's phase angle with respect to the mean for that phase angle for all nights, irrespective of season. With this formulation, possible systematic errors associated with the Moon's geometric albedo have been largely eliminated. In the formulation of equation (7), we minimize the dependence on lunar phase by removing effects, in the mean, arising from the fact that  $p^*$  is a strong function of lunar phase.

[23] In the next step, the data are averaged in time in bins containing 11 nights each to get a mean anomaly for each period. With this method, we cannot derive an absolute measurement of the Bond albedo, but rather we obtain a measurement of its variability.

[24] These seasonal anomalies, which are formulated as fractional changes in  $p^*$ , carry information about variations in weather, climate and surface type. The fractional seasonal variation of the Earth's reflectance over almost 4 years (1999–2002), as determined from our earthshine observations, is shown in Figure 2, together with our

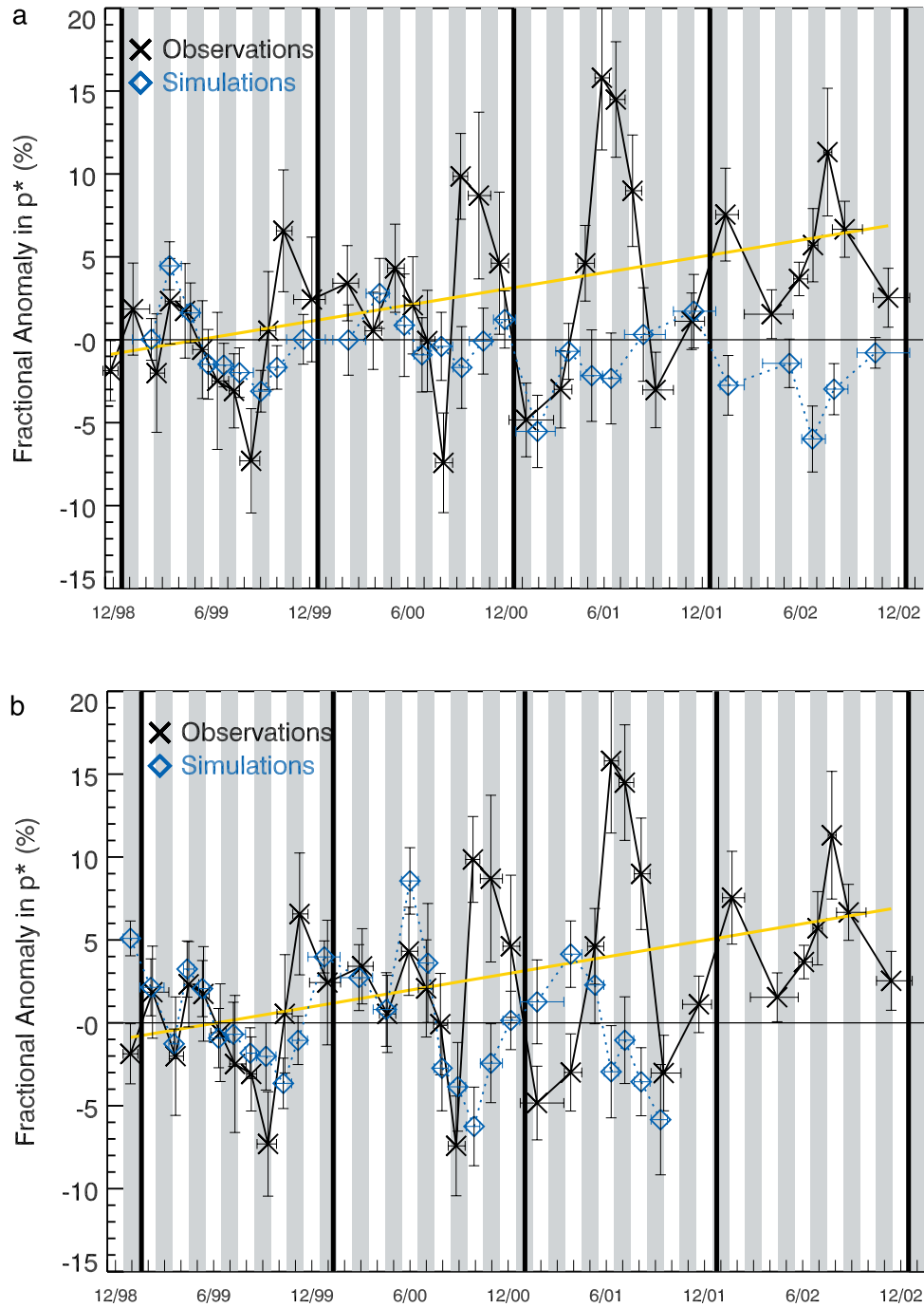


**Figure 2.** Seasonal anomalies in the apparent albedo,  $p^*$ . From December 1998 to January 2003, there are 396 nights of observations, with 11 nights in each of the bins. From January 1999 onward, there are 308 nights for which we have both observations and contemporaneous WSI satellite cloud cover data, which have been averaged in 28 bins with 11 nights in each. We also have ISCCP daily cloud data for the 308 observation nights since December 1998 and ending to September 2001. The crosses show the mean of the observations, with the vertical bars being the standard deviation of the mean. The size of the latter stems from the large night-to-night variations in the cloud cover, rather than from uncertainties in the observations. The horizontal bars indicate the temporal span of each average. The diamonds indicate the corresponding simulated results. Anomalies are with respect to the mean for 1999. The straight line in both panels represents a linear fit to the observational anomalies. (top) Observed anomalies are compared to WSI models. (bottom) Same as Figure 2 (top) but for the ISCCP simulations, which end with the to-date release of those data.

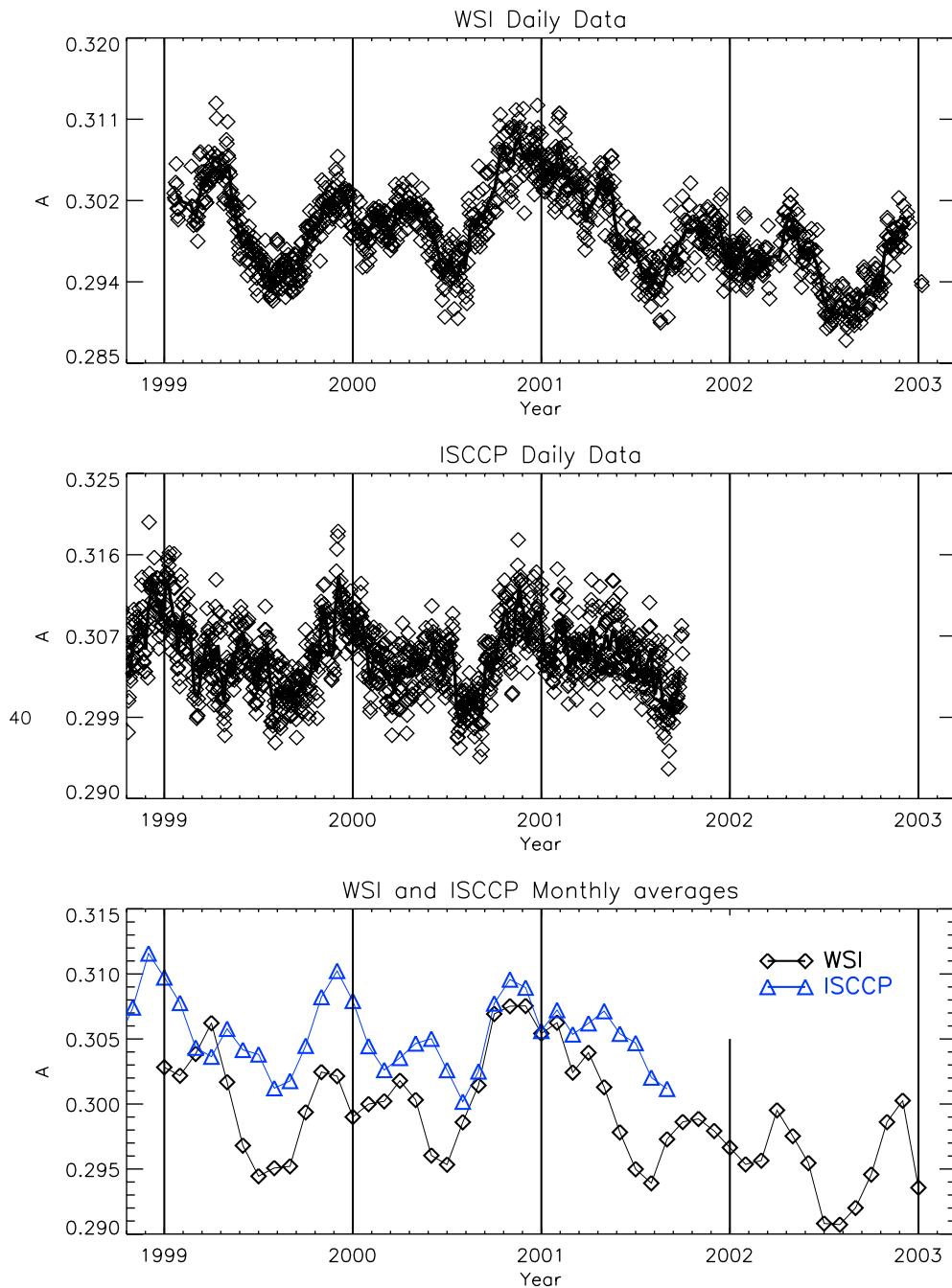


**Figure 3.** (top) Daily mean Bond albedo over the entire Earth, simulated using daily WSI cloud data maps. (middle) Same as Figure 3 (top) but this time using daily mean ISCCP cloud cover maps as input to our models. (bottom) The daily means in Figures 3 (top) and 3 (middle) averaged to monthly values of the Earth’s albedo for the whole Earth (24 hours).

simulations from WSI and ISCCP data. An increasing trend in the albedo of about 1%/year is apparent and significant during the full period of measurements.

[25] One can see in Figure 2 a clear seasonal trend for 1999 and 2000, with the Earth being brightest in the spring in the northern hemisphere and fall generally, when it is also the cloudiest (according to WSI satellite data). We see the seasonal trends in spite of the fact that the variations within each bin are a significant fraction of

the seasonal trends. We emphasize that the large vertical error bars in Figure 2 arise from the large variations in the cloud cover, rather than from any errors in the data. In fact, the variations within each bin are large compared to the formal error bars for any single night. With all of this, we see about 15–20% variation in  $p^*$  from season to season. However 2001 and 2002 do not show the same seasonal pattern. In the early months of the year, they show a dip in the albedo that is also visible in the

simulations (WSI), and it has a maximum in summer time, although this is only reflected by monthly mean ISCCP data (see Figure 4).

[26] Note that the agreement between measured and modeled anomalies is remarkable from the beginning of the measurements until the end of 2000, particularly for the ISCCP simulations, for which all nights coinciding with observations have data available. However, since the end of 2000, although the simulations maintain the same seasonal cycle, the observations start to deviate; we will come back to this point.

[27] The observations show about twice the variability as the simulations, with the differences being greatest at the points with larger departure from the mean. The muted seasonal amplitude of the simulations may well derive from the coarse binning of the scene models and/or the use of simulated snow and ice cover. However, the oversimplified treatment of the clouds is a stronger candidate than any other climate parameter that may contribute to changes in albedo.

[28] In Figure 3, we plot the daily modeled 24-hour Bond albedo simulations for the whole Earth. Figure 3 (bottom) reveals a clear offset between albedos obtained using different data sets. The WSI albedo is significantly lower than the ISCCP one. The computed averaged ISCCP (1983–2001) albedo  $\bar{A}$ , is 0.313 and the WSI (1999–2002) averaged albedo  $\bar{A}$  is 0.300. This difference is well within what we can measure. However, ISCCP data for 1999 and 2000 are the lowest of the 1983–2001 period in cloudiness and albedo,  $\bar{A} = 0.307$ , and so the offset between the two data sets in the common years is reduced by half (0.007). This offset changes with time (Figure 3), even disappearing for short periods. Here we need to remind the reader that the WSI data posted on the Internet are uncalibrated from one day to the next, while the ISCCP data undergo a detailed calibration process.

[29] It is also seen in Figure 3 how the seasonal variation of the two cloud (or deduced albedos) data sets are not equivalent. While the WSI simulations show the expected seasonal variation with an August minimum and November and May maxima [Danjon, 1928; Dubois, 1942, 1947; Gibson *et al.*, 1990], the ISCCP data has a more broad peak during the summer months, which generally increases the albedo for the year. The dominant source of the seasonal variability is the interplay of the annual cycle of cloud cover and snow/ice cover; the land surfaces play only a small role. The seasonal cycle of our modeled 24-hour Bond albedo of the Earth and that of our modeled apparent albedo at the time of observations are closely similar, although the geographical areas contributing to the latter vary slightly through the year due to changes in the inclination of the Earth's and Moon's orbit.

[30] In Figure 4 we have repeated the 24-hour whole Earth simulations of the Earth's Bond albedo, but this time, rather than averaging daily means into monthly means, we have used for our model input monthly mean cloud cover maps given by the ISCCP D2 data set. The observed seasonal anomalies have been also plotted in Figure 4. Note that the ISCCP-derived Bond albedos from Figure 3 and Figure 4 are different, particularly in 2001. It is also striking that during 2001, our  $p^*$  observations do not agree with our

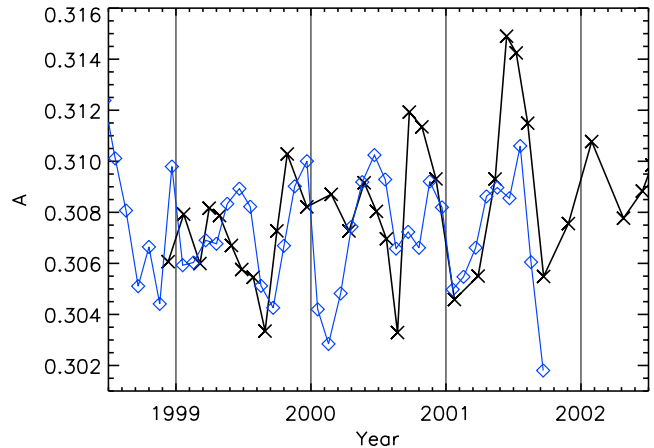


**Figure 4.** Bond albedo simulations of the whole Earth. In this case we use monthly mean ISCCP cloud cover maps as input to our monthly simulation, as opposed to Figure 3, where we used daily values which were then averaged to form a monthly value. The observed seasonal anomalies are overplotted (crosses) and are arbitrarily scaled for comparison. Note the good agreement on both curves for the year 2001.

simulations, but agree with the Bond albedo derived in Figure 4.

## 5. Earth's Bond Albedo

[31] To determine the Bond albedo,  $A$ , from our earthshine observations we need to integrate the apparent albedo,  $p^*(\theta)$ , over all phases of the Moon (see Paper 1):

$$A = \frac{2}{3} \int_{-\pi}^{\pi} d\theta p^*(\theta) f_L(\theta) \sin \theta, \quad (8)$$

where  $\theta$  is the lunar phase angle,  $f_L(\theta)$  is the Moon's Lambert phase function and  $p^*$  is the apparent albedo associated with a particular night (Paper 1).

[32] The kernel of the integrand,  $f_L(\theta) \sin \theta$ , is plotted in Figure 5. Figure 5 illustrates one of the two basic problems in using the earthshine to determine the Earth's Bond albedo. The first, and more significant problem, is that we cannot measure the earthshine for all phases of the Moon. However, it is clear from Figure 5 that this becomes a problem for determining  $A$  predominately for lunar phases near the new Moon. Further, it can be seen in Figure 5 that the integrand in equation (8) peaks near the quarter Moon ( $|\theta| \sim 130^\circ$ ), when the Moon shows a relatively sizable earthshine, while its phase is not so large that the earthshine is visible only briefly near sunset or sunrise. More precisely, to evaluate equation (8) to an accuracy of 0.002 requires data for  $|\theta| \geq 30^\circ$ . Thus earthshine observations for most lunar phases are needed for an absolute value of the albedo, while observations near the full Moon are most sensitive to variations in the albedo because so little of the Earth is visible. The second basic problem in using the earthshine to determine the albedo arises because the orbit of the Moon traces out an ellipse around the Earth, so we cannot measure the earthshine in all directions. Therefore we are insensitive

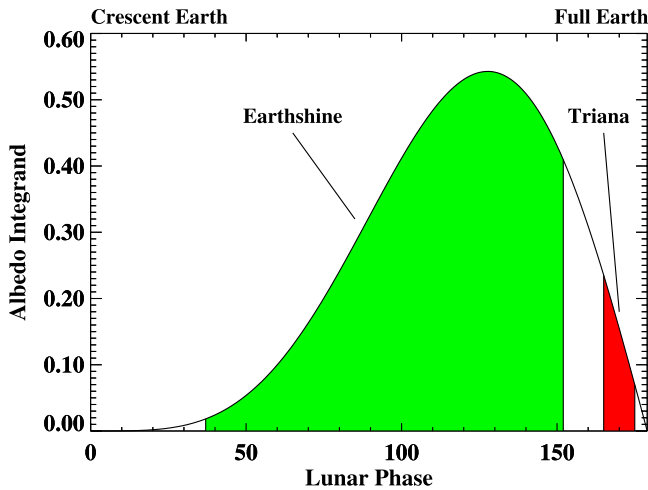


**Figure 5.** The kernel ( $f_L(\theta)\sin\theta$ ) from which the Bond albedo is determined (see equation (8)) shown as a function of lunar phase. Its behavior is dominated by the Lambert phase function for small phase angles and by  $\sin\theta$  for large phase angles. In green we indicate the contribution to the Bond albedo that arises from the range of lunar phases over which we measure the earthshine. In red we show the approximate contribution from a satellite orbiting about L1, assuming the proposed orbit of Triana. If the orbit were to make larger loops around L1, as proposed by M. Lockwood (personal communication, 2002), all phase angles above  $140^\circ$  could be covered.

to any azimuthal anisotropy that might be present in the Earth's reflectance. Later in this section, we use simulations to show that the effect of the anisotropy does not seem to be significant, but it is systematic and one can account for it. We do this by taking advantage of full spatial coverage provided by the simulations.

### 5.1. Determining $A$ From $p^*$

[33] We have a two-step approach to determining the Bond albedo from the earthshine apparent albedos. The first step is utilizing the simulations. Simulations for the 3 years of data for all nights that we have cloud cover are shown in Figure 6 (including all phase angles). Figures 6 (left) and 6 (right) show the same data. In Figure 6 (left), we show a least squares fit in which the apparent albedo is determined for 180 bins of  $1^\circ$  apiece. The least squares fit is made using

$$\chi^2 = \frac{1}{(N - N_f)} \sum_{j=1}^N \left( \frac{\Delta p_j^*}{\sigma_j} \right)^2, \quad (9)$$

where  $N$  and  $N_f$  are the number of nights simulated and the number of degrees of freedom in the solution, and where  $\Delta p_j^*$  and  $\sigma_j$  are the deviation of  $p_j^*$  from the fit and the error in the determination of  $p_j^*$ , respectively. There are oscillations at short angular scale in  $p^*$ , which are largest at the extreme phase angles. The extreme phase angles do not contribute to the Bond albedo, which is  $0.2939 \pm 0.0001$  for the least squares fit. The oscillations are an unpleasant artifact of the least squares method. We could,

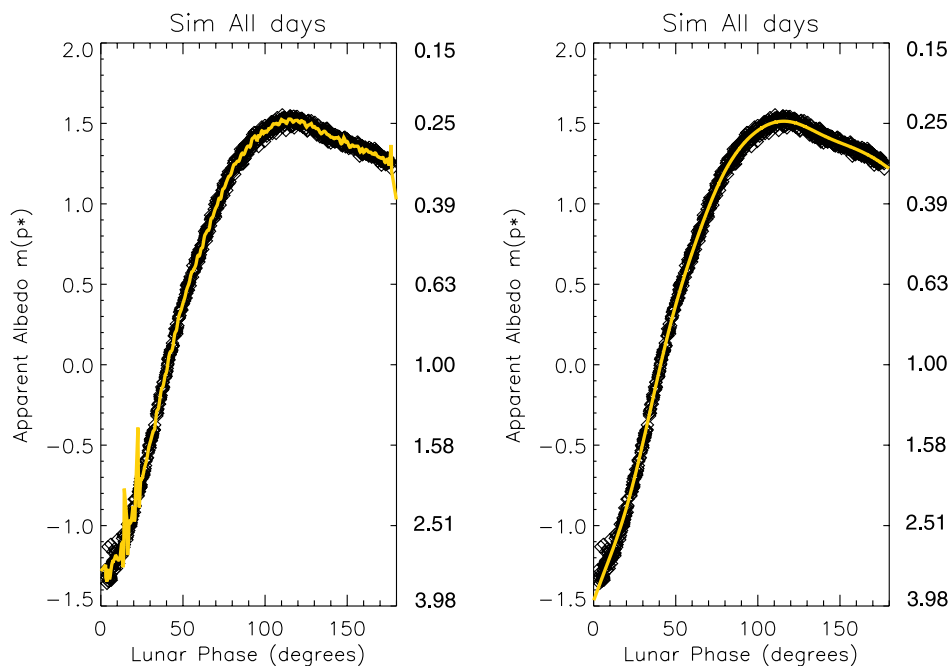


**Figure 6.** Each simulated, single-night whole Earth apparent albedo is represented by an empty box. Since there are 898 nights, individual boxes cannot be resolved. The nights span the period from December 1998 to March 2002 and are the nights for which we have cloud cover data. (left) A least squares fit to the data is shown, with the apparent albedo being determined in individual bins that are  $1^\circ$  wide. Note the oscillations at short angular scale for all phase angles. (right) The regularized fit to the same data. On the right-hand  $y$  axis, we use units of  $p^*$ .

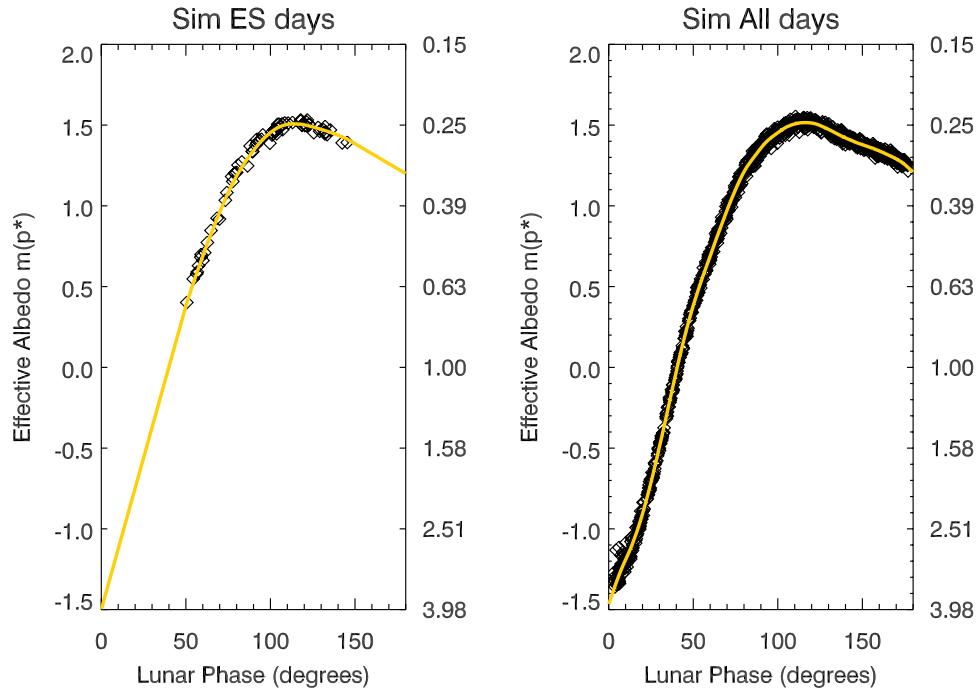


**Figure 7.** Boxes representing a whole Earth (i.e., covering a 24-hour period) simulated albedo. (left) Whole Earth simulations for which the 24-hour period includes nights for which we have earthshine data and cloud cover (268 nights). The 268 nights span the period from December 1998 to March 2002. (right) Whole Earth simulations for all 24-hour periods, during the same period, for which we have cloud cover data (898 nights: 466 during the waxing Moon and 432 during the waning phase). The yellow curve is derived from the constrained or regularized least squares fit to the left panel. On the right-hand  $y$  axis, we use units of  $p^*$ .

instead, perform a least squares fit with a low-degree polynomial, which would suppress the oscillations. However, the meaning of the stiffening would be unclear. We believe that the apparent albedo should be a smoothly varying function, and we impose this in a mathematically meaningful way, regularization [Goode, 1995], in which we minimize

$$\chi^2 \left(1 - \frac{N}{N_f}\right) + \lambda \int_{-\pi}^{\pi} \left[ \theta^2 \frac{d^2}{d\theta^2} \left( \frac{\Delta p_j^*}{p^*} \right) \right]^2 d\theta, \quad (10)$$

where  $\Delta p_j^*$  is the difference between the  $j$ th data point and the fit to the data (the quantity we are determining) in Figure 6 (right), while  $\lambda$  is the regularization parameter which is, in reality, a smoothing constraint. In principle, the parameter is adjusted until  $\chi^2$  per degree of freedom is unity, so that the errors in the data are converted to comparable errors in the fit. However, the  $\chi^2$  space is relatively flat, so one typically weakens  $\lambda$  until oscillations at short angular scale almost begin to appear in the fitted  $p^*$  function. Other forms of the constraint are certainly possible, but a second derivative constraint seems to work best here. In applying the regularization to Figure 6 (right), we have the advantage of being able to directly compare the obtained value of  $0.2937 \pm 0.0003$  to that obtained by simple least squares ( $0.2939 \pm 0.0001$ ). The two results are consistent, and known with about an order of magnitude greater precision than we have been discussing for the

observations. The error in the Bond albedo from regularization is about three times greater than that from the least squares determination. This is due to the unphysical variation introduced by the short angular scale variations in the least squares fit. Still, the regularization introduces a point-to-point correlation in the errors, but we shall see that this effect is small, and the errors very nearly take the standard meanings.

[34] Note that in Figure 6 we have observations for all lunar phase angles, averaged over the whole day, which give us a large number of points and a small spread of the modeled values, as our models are overly smooth. Hence our determination of the albedos with such small error in the integration. Those errors do not correspond to our measurement precision for the albedo from observations. The measurement errors are about an order of magnitude larger.

[35] Next, we apply regularization to the subset of nights shown in Figure 7 (left), and using essentially the same regularization parameter as in Figure 6, and after assuming that the left panel and right panel have the same values at phase angles of 0 and 180°. Figure 7 (left) is the subset of 24-hour simulations for which we have observational data taken on the same calendar day. The resulting fit is shown in Figure 7. It can be seen that the fit to the subset of the data fits the whole of the data quite well, especially for the range of phase angles that is so important in determining the Bond albedo. With this fit, we find a Bond albedo of  $0.298 \pm 0.001$ , which we regard as being consistent with the pure

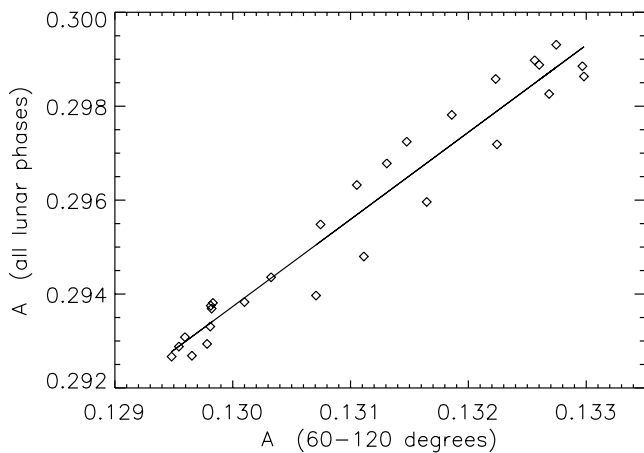


**Figure 8.** Scatterplot of the mean Bond albedo for whole Earth simulations, integrated over all lunar phases angles, and the integration value over lunar phase angles from 60° to 120° only. Each point is a 12-month mean, starting with the period December 1998 to November 1999 for the first point, January–December 1999 for the second, and so on until April 2001 to March 2002 for the last point. The correlation coefficient between these two integrations is 0.98.

least squares and regularization results of Figure 6, after recognizing the fact that 2/3 of the nights in Figure 7 (right) are absent in the left panel. The fit is fairly insensitive to the choice of  $\lambda$  over nearly an order of magnitude.

[36] The second step in determining the Bond albedo for the observations is a further effort to account for the fact that the observational data do not span all phase angles. For this, we next examine the  $p^*$  simulations for the daytime region of the Earth visible from the Moon, for phase angles between 60 and 120°, the regime for which we have the most confidence in the data. In Figure 8, we show a scatterplot of the Bond albedo for a 12-month running mean versus the contribution to that integral coming from phase angles between 60 and 120°. To construct the 12-month running mean, we start from the period December 1998 to November 1999 and then remove the first month and add a new one until the period April 2001 to March 2002. The correlation between the total and “partial” integration values is 0.98. To test this method we have repeated it using the interval 90°–120°, and we get a correlation between total and “partial” integration of 0.99. The linear fit gives us a way of converting a partial integral to a total integral. The albedos obtained by converting the partial integrals and from the total integrals are practically indistinguishable. After experimentation, we find that this approach returns more reliable values for the albedo than a simple regularization fit as used here in Figure 7 (left) and in *Goode et al.* [2001].

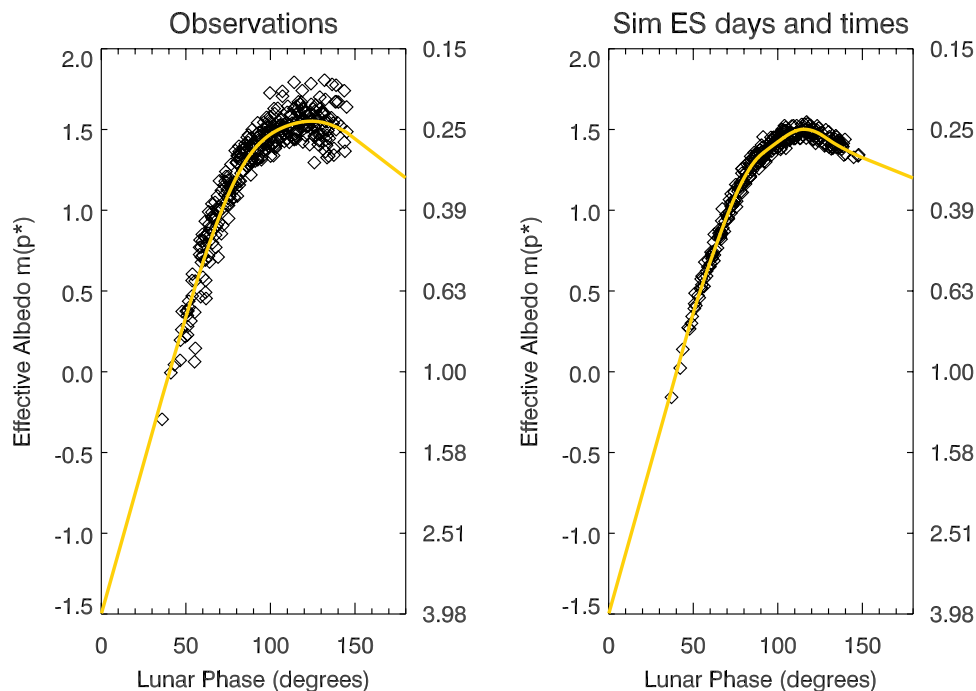


**Figure 9.** (left) Observed  $m(p^*)$ s plotted against the absolute value of the lunar phase from 225 clear observing nights from December 1998 to March 2002. (right) Simulations shown covering the time intervals and parts of the Earth that contribute to the earthshine signal for the 268 nights for which there were observations and contemporaneous cloud cover data. Each data point represents a nightly average of a series of 0.5–3.0 min earthshine measurements taken once every 5 min with 0.1–5.0 s moonshine observations interspersed. Error bars for each night would be within the symbols. For the 268 nights for which we have observations and simulations, constrained least squares fits to the data and simulations are shown by the yellow curves. On the right-hand  $y$  axis we use units of  $p^*$ .

[37] We next use this linear relation to determine a Bond albedo from the observational data. Again, we use the daytime Earth's region visible from the Moon simulation points at 0 and 180° to fix the regularization, and then determine the Bond albedo by scaling the fit between 60 and 120° by the same linear factor as used in determining the Bond albedo for the simulations at all available lunar phases. Applying the same regularization to the observational data (see next section), which contains as a subset the 268 nights in Figure 7 (left), over a 3+ year period we find the mean Bond albedo for the Earth to be  $0.295 \pm 0.002$  ( $0.293 \pm 0.003$  for the evening observations and  $0.296 \pm 0.002$  for the morning). The deviations will contain not only the noise, but also any seasonal and long-term albedo variability that might have occurred during this period. The fit is shown in Figure 9 (left). Figure 9 (right) shows the corresponding fit for the simulations covering the same times and parts of the Earth that contribute to the earthshine, for which we calculate an albedo of  $0.298 \pm 0.001$ . The larger deviations in the observational results are indicative of the greater spread of the observational points about the mean (compare the left and right panels of Figure 9).

[38] One of the prices paid for using regularization is that the point-to-point values of the solution are correlated, implying that the meaning of the errors is somewhat damaged. The damage is reflected in errors that are smaller than they are in reality. For instance, if the constraint were dominant, the uncertainty at each point in the solution would be the standard deviation of the mean. To ascertain whether the uncertainties quoted in this section are significantly too small, we also determined the errors in a completely different way, which does not suffer from the limitations imposed by regularization, and reveals that they are not significantly too small (section 5.4).

## 5.2. Effect of Anisotropy

[39] As mentioned at the beginning of this section, one concern about measuring the earthshine to precisely determine the Earth's albedo is the amount of anisotropy in the Earth's scattering. At any instant, the Moon subtends  $0^\circ.5$  as seen from the Earth, and the obliquity of the Moon's orbit extends this coverage over the lunar month to only  $6^\circ$  on either side of the ecliptic; thus earthshine is not sensitive to light scattered out of the ecliptic. We can directly test the sensitivity by comparing the result of simulating the Bond albedo for the whole Earth to that using the simulated earthshine. For the case of the Earth that is in the sunshine, we use equation (4) and calculate an average for the more than 3 years of data,  $A = 0.3001 \pm 0.0002$ . For the whole of the Earth in the earthshine, we are effectively assuming that for all lunar phases the earthshine does not depend on the azimuthal scattering angle. We test equation (8) by using  $p^*(\theta)$  from the least squares fit in Figure 6 (left), from which we determined an equivalent 3+ year average Bond albedo of  $0.2939 \pm 0.0001$ . The discrepancy arises because the relatively brighter polar regions are sometimes in the sunshine, but not in the earthshine. For this reason the Bond albedo values obtained from our earthshine observations and our  $A^*$  simulations should be increased by 0.006. This effect

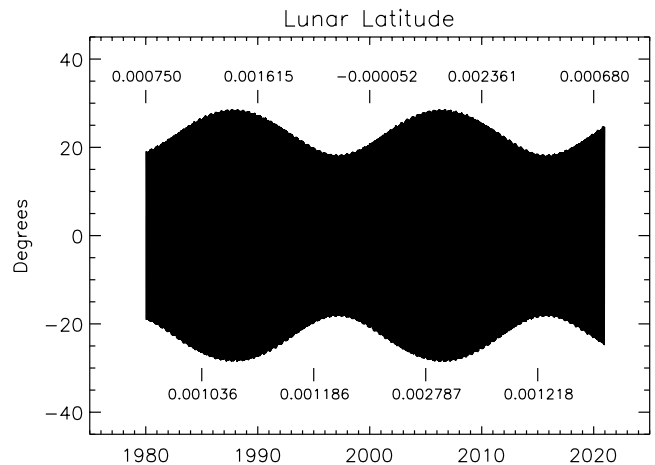


**Figure 10.** Precession of the Moon's orbital plane with a period of 18.6 years inducing a corresponding periodicity in the Earth's albedo as deduced from earthshine. The figure shows simulations for the period 1980–2020, using 25 January 1999 cloud cover data as though all nights were “frozen” in time with the same cloud cover. Also indicated, for some of the years, are the mean annual changes in Bond albedo with respect to the albedo for 1999, caused solely by the evolving lunar declination. The albedo was simulated using equation (8). During any small time interval the position of the Moon changes but within the limits defined by the envelopes to the plot. Thus the monthly changes give rise to the smeared appearance within the envelope.

is illustrated in Figure 1 (right) for which the Moon is northerly in the sky and doesn't receive light from the sunlit southernmost regions of the Earth.

[40] However, it could be that our models are not accurate enough to detect any anisotropy bias. Thus the possibility of an anisotropy bias in the earthshine measurements remains and needs to be explored in future work.

## 5.3. Precession of the Lunar Nodes

[41] A higher order difficulty in determining the Earth's reflectance from the albedo is that the intensity of the earthshine varies with the precession of the lunar nodes. That is, because the gravitational effects of the Sun and Moon are not always the same, there is some wobble in the motion of the Earth's axis; this wobble, called nutation, causes the celestial poles to move, not in perfect circles, but in a series of S-shaped curves with a period of 18.6 years. This precession of the Moon's orbital plane has a period of 18.6 years. The sensitivity of the earthshine arises from the anisotropy of the light scattered by the Earth. For example, when the declination of the new Moon is a maximum (some  $29^\circ$ ), and it is near the northern-summer solstice, more of the arctic polar ice cap is visible and the earthshine will be brighter. Some 9 years later, the lunar declination under the same conditions will be only  $18^\circ$ , and the earthshine will be at a minimum. We have performed simulations to study this effect and the results appear in Figure 10 and the Table 1. It is clear from Figure 10 that the nutation of lunar nodes perturbs  $p^*$  at the 0.0012 level or less, or about five times smaller than the effect of anisotropy. It is straightforward,

**Table 1.** Effects of the Nutation of the Moon's Orbital Plane Comparing Similar Times and Different Epochs

Span of Years	$A$	$\Delta A/A$ , %
Jan. 1996 to March 1998	0.29453	$[A(3) - A(1)]/A(1) = 1.1$
Jan. 2002 to March 2004	0.29612	$[A(2) - A(1)]/A(1) = 0.7$
Jan. 2008 to March 2010	0.29623	$[A(3) - A(2)]/A(2) = 0.3$

but necessary to account for this in comparing earthshine results from different epochs.

#### 5.4. Alternate Determination of Uncertainties in the Bond Albedo

[42] In calculating the Bond albedo, we have an alternative way to connect the precision to which we determine the  $m(p^*)$  to the accuracy to which we determine  $A$ . To do this, we use the daily WSI cloud cover maps and calculate the whole Earth albedo  $A$ , the apparent Earth's albedo  $m(p^*)$  and the variation of each during the full day and during the times for which we have earthshine observations. For the calculations, we use a third-order polynomial fit to  $m(p^*)$ , which defines a mean calculated apparent albedo for the Earth,  $m(p^*(\theta))$ , and residuals,  $\Delta m(p^*)^{\text{calc}} = m(p^*) - m(p^*(\theta))$ ; the latter carry information about the weather, climate and surface type. Their correlation with the calculated global albedo anomalies ( $\Delta A = A - \bar{A}$ ) at the times at which earthshine observations have been taken, is shown in Figure 11 (top), where we have included the 268 nights for which we have simultaneous cloud cover data and earthshine observations.

[43] For the observational data, we make a scatterplot during the same periods, and assume they correlate with  $\Delta A$ , as shown in Figure 11 (bottom). In detail, we used a third-order polynomial fit to define a mean observed apparent albedo  $m(p^*(\theta))$  and observed residuals  $\Delta m(p^*)^{\text{obs}}$ . Their correlation with the global calculated

albedo anomalies ( $\Delta A = A - \bar{A}$ ) is shown in Figure 11 (bottom) including a linear fit to the points. Figure 11 gives us insight into how accurately we can measure the albedo. The large number of points in Figure 11 (bottom) comes from the fact that in order to make a direct comparison, we interpolate our 30-min resolution  $\Delta A$  from simulations for each time at which an observation is taken (a period between 0.5–3.0 min). Whereas in Figure 11 (top), a direct comparison between  $\Delta A$  and  $\Delta m(p^*)^{\text{calc}}$  is done. The correlations are  $-0.66$  and  $-0.27$  in the top and lower panels respectively, both significant at higher than a 99.99% confidence level.

[44] Using Figure 11, we note that a variation in  $A$  of 0.01 corresponds to changes in  $m(p^*)^{\text{obs}}$  of  $0^m.043$  (or 4.0% in the observed  $p^*$ , using  $\delta m(p^*) = (\ln 10 / -2.5)(\delta p^*/p^*) = -1.08(\delta p^*/p^*)$ ) and to a change in  $m(p^*)^{\text{calc}}$  of  $0^m.078$  (or 7.2% change in the calculated  $p^*$ ). Equivalently, a 1% earthshine measurement of  $p^*$  determines the albedo with a precision of 0.0025. To place this precision in context, we note that independent satellite determinations of the monthly mean albedo can differ by 0.005 or more, and that the seasonal range of the monthly mean albedo is 0.015 or more (see Figure 2). The individual simulated points have error bars of about 0.005 and the seasonal variations have an amplitude of 0.027.

[45] Our nightly sigma  $\sim 2\%$  observational uncertainty in each nights measurement of  $p^*$  corresponds to a deviation in of  $\sim 0^m.02 m(p^*)$ , which implies measuring  $A$  to  $\pm 0.005$ . This value is comparable to that from satellite data [Kato et al., 2002]. From Figure 11, we converted the error in  $m(p^*)$  into the error in  $A$ , which averaging over a year, implies measuring  $A$  to slightly better than 0.005 (or to about 0.003 over 3 years), even though we have observed about a third of the nights in the year. These uncertainties are similar to those we determined using constrained least squares for  $A$ . Thus we conclude that

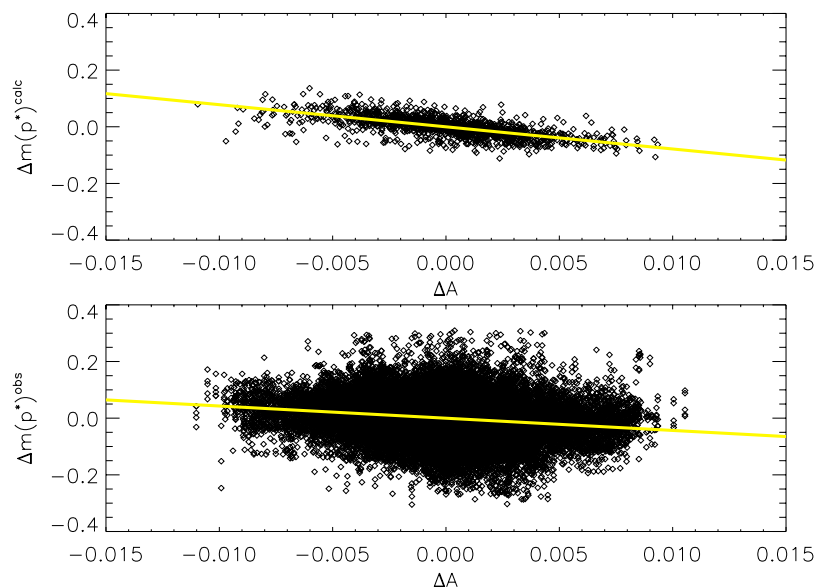


**Figure 11.** (top) Linear correlation of the calculated earthshine anomaly,  $\Delta[A^*]^{\text{calc}}$ , with the calculated global albedo anomaly,  $\Delta A$ , for 1694 calculations for lunar phase angles for which  $140^\circ \geq |\theta| \geq 40^\circ$ . (bottom) Linear fit to observational anomalies,  $\Delta[A^*]^{\text{obs}}$ , during the same time periods, assuming  $\Delta A$  is the same as that from the calculations.

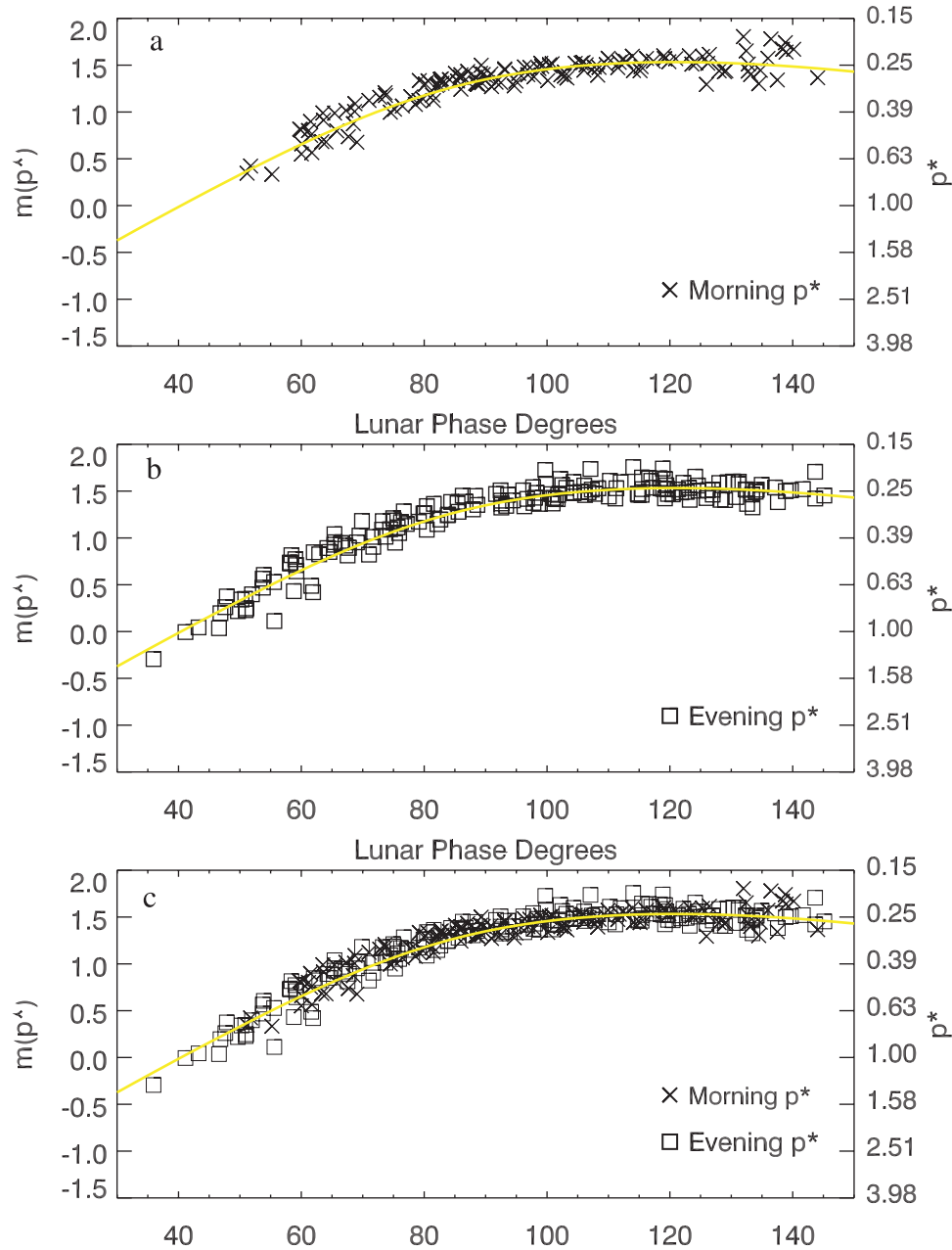


**Figure 12.** Plot of the mean  $m(p^*)$ , which is determined from 25 sets for each night, for (a) morning and (b) evening observations. (c) The combined results for mornings and evenings. 340 nights of observations are included (150 nights of morning observations and 190 evening). Solid lines indicate the curve from the fit to the data in the bottom panel. On the right-hand  $y$  axis we use units of  $p^*$ .

the regularization has not underestimated the uncertainties in a meaningful way.

## 6. Bond Albedo During 1999–2002

[46] Figure 12 illustrates the change in  $m(p^*)$  against lunar phase angle as determined from the nightly earthshine observations, with the morning and evening observations presented separately, and combined. In the plots, each data point represents a nightly averaged  $p^*$  value, with which we study the changes in  $p^*$  for different nights, months and seasons. One may first note that while  $p^*$  is relatively flat

near the quarter Moon, the flatness implies a near-Lambertian Earth for most lunar phase angles (see equation (10) of Paper 1). However, with the Moon approaching full phase and  $\theta$  getting close to  $180^\circ$ , the Earth as seen from the Moon, becomes a thin crescent, and so Earth-reflected radiation reaching the Moon is more dominated by forward scattering in the atmosphere. For lunar phase angles much below about  $40^\circ$ , we presently regard the results as unreliable because of the proximity of the earthshine fiducial patches and the terminator (the transition from the moonshine to the earthshine is not sharp). Further, we do not have reliable earthshine data near the new Moon (much beyond a

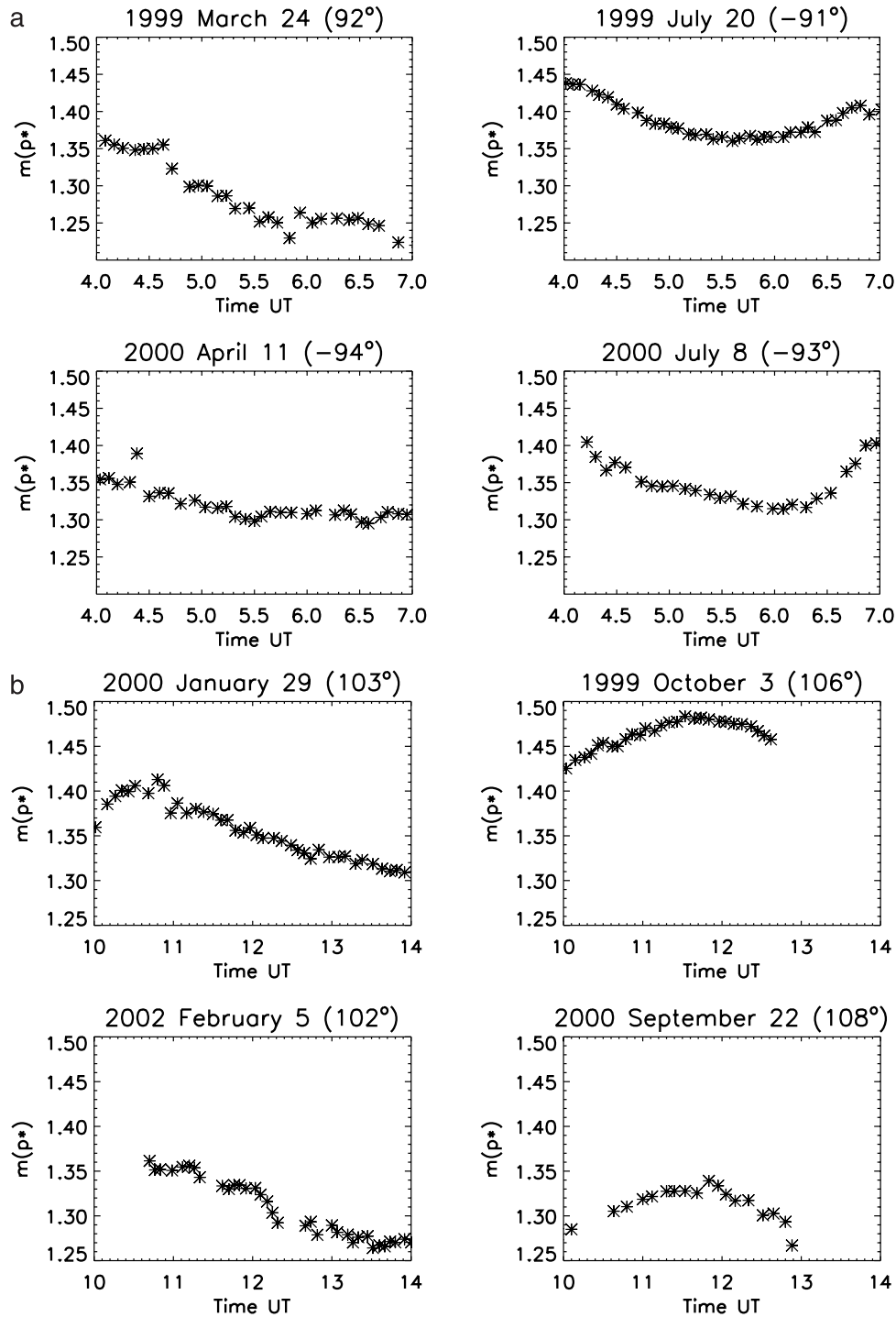


**Figure 13.** Plots of  $m(p^*)$  observed for several nights of data, against the time of observations (0000–2400 UT). The values are derived for the fiducial pair used by *Goode et al.* [2001]. (a) All nights have almost equal lunar phase angle. Note how the variability along the night is the same in all panels, but the mean value depends on the seasons. Note also that the two right panels correspond to the same month (July, 1 year apart) and have almost equal values. (b) The difference in lunar phase angle between the right and left panels is quite small ( $\sim 5^\circ$ ), but it is enough to make the nightly variation slightly different (or delayed). Again, the average albedo value depends on the season.

lunar phase angle of about  $140^\circ$ ) because the earthshine is visible for only a brief time near sunset or sunrise, depending on whether the Moon is in its waxing or waning phase. Thus our earthshine observations at lunar phase larger than

$140^\circ$  are made at large air mass and the extrapolation to zero air mass is unreliable (see Paper 1). For large lunar phase angles, it is also difficult to find a fiducial patch that is confined inside the thin Moon crescent.

[47] A detailed examination of Figure 12 reveals that, with respect to the fitted mean, the  $p^*$  determined from the local Big Bear Solar Observatory (BBSO) morning observations (lunar phase angle  $> 0$ ) are not apparently distinct from those determined from the local evening observations (lunar phase angle  $< 0$ ); that is, the earthshine data from BBSO nights implies that the contemporaneous sunlit parts of the Earth are equally shiny in the evening and in the morning (note that evening and morning refer to local time at BBSO). Ultimately, we determine from the earthshine data a mean albedo of  $0.293 \pm 0.003$  for the evenings and of  $0.296 \pm 0.002$  for the mornings. The lack of a significant difference may seem somewhat surprising because the earthshine we observe in the mornings and in the evenings comes from the reflection of sunlight from different parts of the Earth. In our evening observations, the earthshine is dominated by southeast Asia. In the mornings, the earthshine is dominated by Africa, Europe and the Atlantic.

[48] One might think that the agreement between evening and morning determinations results from fortuitous compensations from the afternoon/evening development of deep convection versus morning maxima of low stratified clouds. However, most likely, the agreement is due to the large area-average in our earthshine Bond albedo integrations, which contains a wide mix of different land, ocean, ice and cloudy areas.

[49] Bearing in mind that a change in  $m(p^*)$  of  $0^m.01$  corresponds to about a 1% change in  $p^*$ , we observe a roughly  $\pm 5\%$  variation within a season in the apparent albedo,  $p^*$ , even near the quarter Moon where the data are most reliable. This variation is primarily associated with changes in the cloud cover and/or changes in the lunar phase, rather than some error in the data collection/reduction process. In Figure 12, the spread about the mean is even larger, this is primarily associated with seasonal and long-term variations in the reflectance (Figures 2 and 3).

[50] To better understand the influence of the Earth's varying topography and cloud cover on  $p^*$ , we plot the albedo as observed throughout single nights in Figure 13. This plot comes from using equation (2) after each point is corrected for air mass and inputting the proper lunar phase for each observed time point. Note that the lunar phase function changes by about  $0.5^\circ$  per hour. In Figure 12, each point represents the mean of a single night. In each panel of Figure 13, the mean for the night is given as a number. In Figure 13a, observations of four nights with almost the same lunar phase, but from different months, are compared. They demonstrate a common tendency of an early decrease in  $m(p^*)$ , or a brightening Earth, as the Sun is rising over Asia, increasing the contribution from the relatively bright Asia. The sun rising over a cloudy Asia causes a 5–10% change in  $p^*$  over the period of the observations. Even though the temporal evolution of the points in Figure 13 closely resemble each other, the mean value of  $p^*$  changes as much as 5% or more from night to night. This difference reflects a greater Asian cloud cover on 24 March than on 20 July. However, the fact that daily and seasonal variations are mixed makes the analysis difficult. Some part of the appreciable difference is probably due to seasonal changes in cloud cover rather than to differences in the part of the world we are measuring. In Figure 13b the observations are from four mornings at similar phases of the moon, covering

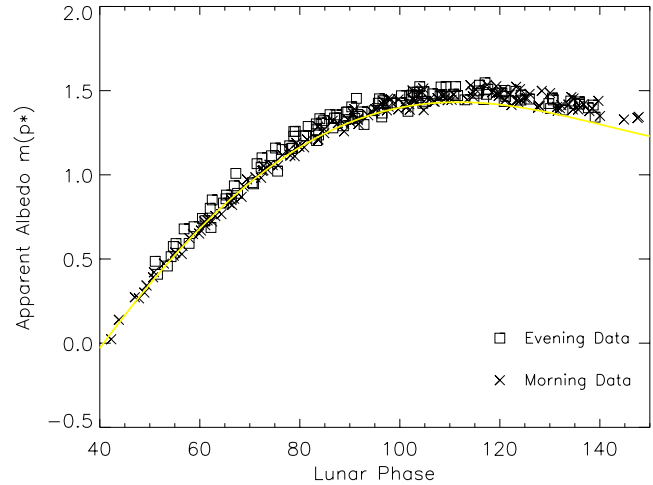


**Figure 14.** Plot of  $m(p^*)$  versus the absolute value of the lunar phase from simulations covering the same phases of the Earth as the observational results in Figure 12; that is, the simulations are looking at the regions of the Earth visible from the Moon at the times of our earthshine observations. Each data point represents the averaged  $m(p^*)$  value throughout 1 night; crosses indicate a morning observation (lunar phase  $> 0$ ) and squares indicate an evening observation (lunar phase  $< 0$ ). For reference the solid curve shown is fit to the data in Figure 12.

comparable local times. Figure 13b (right) show an increasing  $m(p^*)$ , or a darker earth, as time goes on. This is because the sunrise over the Atlantic is increasing the role of the darker, and less cloudy, ocean in the earthshine.

[51] As shown in Paper 1 for a single night, if we combine nights to obtain, say, a yearly average, then the total deviation, from all sources of uncertainty, will be smaller, but no smaller than that associated with the mean values of the various lunar phase functions and the ratio of the geometrical albedos. For instance, we have 340 nights of data for which the fit to Beer's Law has a standard deviation of less than 1% for the single pair of fiducial patches used by *Goode et al.* [2001]. We regard these as our "good" nights. If we calculate the standard deviation of the mean for the 150 (190) mornings (evenings) pairs, we find 0.8% (0.7%). Combining this with the uncertainty in the lunar phase, we find a deviation of less than 1% in the binned  $p^*$ 's. Such error bars would be well within the symbols of Figure 12. The most likely source of systematic errors is the determination of the geometrical albedos, coming from a single lunar eclipse, but such systematic errors would not change the spread in the points. If the presumed systematic errors were comparable to the measurement errors we can reasonably identify, they are still considerably smaller than the spread in the  $m(p^*)$ 's that appear in, say, Figure 12.

[52] In Figure 3, we showed daily mean global albedos from our simulations of the whole Earth covering 1999.0–2002.3, and calculated using equation (4) and WSI daily cloud maps. Roughly, Figure 3 shows peaks in the Earth's reflectivity in the fall and spring, while showing minima in the winter and summer. From this, we determine a mean Bond albedo of 0.3 over that period. We note that the size of

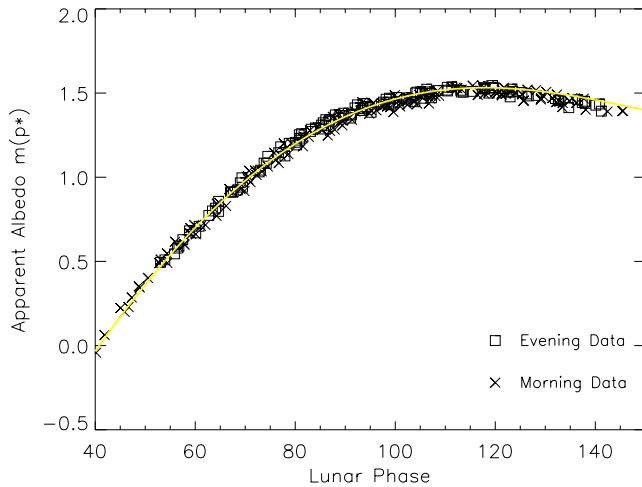


**Figure 15.** Plot of  $m(p^*)$  versus the absolute value of the lunar phase from simulations covering the whole Earth for all days for which we have observations. Each point represents the 24-hour average of UT-defined days for which we have earthshine data. The crosses and squares are given to show whether the 24-hour average is connected to observations at positive or negative lunar phase. For reference the solid curve is the fit to the data shown in Figure 12.

the spread in night-to-night variations is comparable to the amplitude of the seasonal variability.

[53] Applying equation (6), we also simulated the observed apparent albedo shown in Figure 12 covering the same parts of the Earth at the same time. The results are shown in Figure 14. Note that the distribution is tighter to the fit than in Figure 12. Thus the greater scatter in Figure 12 cannot be due to different nights for the same lunar phase seeing different parts of the Earth, because each night's simulation covers exactly the parts of the Earth which are observed. However, like the observational results, there is no clear distinction between the simulations for morning and evening. As in Figure 12, it is also clear from the simulations shown in Figure 14 that the evening data have a greater scatter about the mean than do the morning data. This implies a more variable cloud cover over Asia. In Figure 15, we show the same kind of plot as Figure 14, but covering the entire Earth for nights for which we have observations and cloud cover data (see the difference in coverage between the solid lines and solid boxes in Figure 1). Since the whole Earth simulations average more of the globe, it is not a surprise that these simulations show considerably less scatter than those of a part of the Earth. We also note that the mean apparent albedo in our simulations, is higher for the whole Earth than it is for the part we see by  $0.016 \pm 0.017$  (1.3%) in  $p^*$ ; that is, the albedo increases when we add the third of the Earth invisible to Big Bear. That may be a consequence of including the American land mass, although the result is not statistically significant.

[54] We next consider how the results could change with a quite different lunar phase function, like that of Danjon.

### 6.1. Comparisons With Danjon's Results

[55] To compare our results with those of *Danjon* [1928, 1954], we show our data in Figure 16, but analyzed using

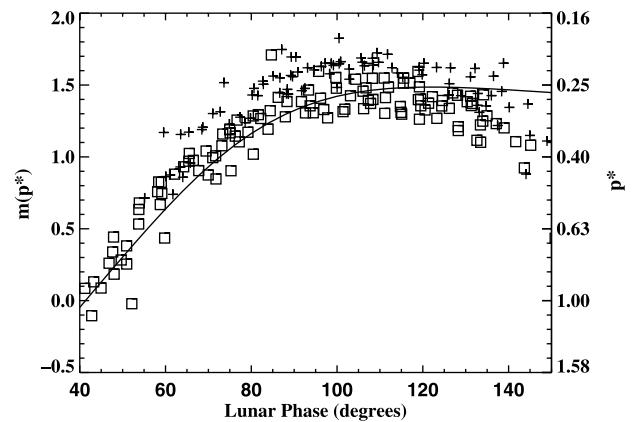


**Figure 16.** Danjon's lunar phase function (see Figure 12 in Paper 1) used to analyze our observational data. The solid curve is the regularized fit to the same data analyzed using our lunar phase functions, as in Figure 12. The points shown are those derived using Danjon's phase function. Since Danjon's phase function is systematically lower than the correct one for phase angles that make the largest contribution to  $A$ , this explains how Danjon derived an albedo of about 0.4 from his observations, which is much higher than our observed and simulated values of about 0.3.

Danjon's phase function (as shown in Figure 13 of Paper 1). In Figure 16, the solid line shown is the fit from Figure 12, which is for the same nights, but analyzed with our phase function. Clearly, for phase angles below  $100^\circ$  the data tend to lie above the fit, while for phase angles above  $100^\circ$  the points tend to lie below the fit. To understand why Danjon found a Bond albedo about 0.1 larger than the true value, one must also inspect the kernel from which the Bond albedo is determined, see Figure 5, where the kernel peaks at about  $130^\circ$  (near the quarter Moon). These phases are most significant in the determination of the albedo. Thus the inconsistency between Danjon's albedo of about 0.40 and our observed value of 0.30 comes mainly from Danjon's underestimate of the lunar opposition effect [Flatte *et al.*, 1991; MacDonald and Koonin, 1992], which carries over into the significant overestimate of the lunar phase function near the quarter Moon that dominates the determination of the albedo.

### 6.2. Interannual Changes in the Albedo

[56] At the present rate of earthshine measurement from our single station, we realize that we cannot determine a

**Table 2.** Mean Annual Albedos for Each of the Years Available in the Earthshine Record<sup>a</sup>

Year	Mean Albedo	$\sigma$	Error, %	Days
1999	0.297	0.003	1.0	117
2000	0.310	0.003	1.1	105
2001	0.306	0.003	1.1	89
2002	0.309	0.005	1.5	75
1999/2001	0.301	0.002	0.6	311

<sup>a</sup>Also given are the standard deviation of the mean, the percentage deviation (or error), and the number of nights involved in each albedo determination. The mean value for the period 1999/2001 is also given. Note that a value of +0.006 has been added to all the albedos to account for the polar regions (see section 5.2).

precise monthly albedo without a global network. For this reason, we concentrate our efforts here on calculating annual albedos for each year of available data, following the methodology discussed in section 5. The results are tabulated in Table 2. Since 1999, year-to-year changes in the Earth's albedo of order of 3–4% are observed.

[57] A series of straightforward corrections are applied to our daily  $p^*$  measurements (see Paper 1), so that our Bond albedo measurements are insensitive to natural variations, such as astronomical distances or lunar libration. Also, included is the systematic effect of the polar regions that are sometimes in the sunshine, but not in the earthshine. Since the polar regions are quite shiny, we must add 0.006 to the earthshine values. Only the effect of lunar precession of the plane of the Moon's orbit is not included. This effect serves to increase the measured Bond albedo from 1999 to 2000, from 2000 to 2001 and from 2001 to 2002. However, during this period, the effect is at least an order of magnitude smaller than the observed year-to-year changes.

## 7. Conclusions

[58] From BBSO, we have observed the earthshine for more than 3 years. We determined a large-scale average of the Earth's albedo for major areas of the Earth, including Europe, Africa and the Atlantic Ocean in our morning observations, when the Sun is high over Africa and the Atlantic Ocean, and the Moon is in its declining phase. We also measured the albedo for large areas in southeast Asia and the Pacific in our evening observations during the rising phase of the Moon. From the earthshine data, we see that southeast Asia and West Africa/Southern Europe have very nearly the same albedo.

[59] We have learned that the albedos we determine are as precise as determined from satellites. Thus the earthshine method provides a different way to measure the Earth's albedo. One of the obvious advantages of earthshine observations is having an absolute calibration coming from the bright side of the Moon. This is because we make use of relative photometry as opposed to satellite instrumentation, which normally make use of absolute measurements, more prone to calibration errors.

[60] We have compared our results with models of the Earth's scenes inputting contemporaneous snow/ice cover from models and cloud cover from satellites. We find a general agreement between the observed and modeled results, with the model results uniformly showing milder amplitude variations. The greater spread of the observations, such as seen in Figure 12, does not result from errors in our observations, but rather from seasonal and long-term changes in reflectance that are not captured by our models. In sum, we conclude that our models, using daily mean cloud cover and a simplified model of the cloud radiative properties, are overly smoothed.

[61] With our level of precision, we can track long-time frame changes in the Earth's albedo, if they are at a climatologically significant level. Both from our observations and simulations we have found strong seasonal variations and annual increasing trend during the 1999–2002 period.

[62] **Acknowledgments.** The authors would like to thank the several anonymous referees for their comments and ideas which led to the improvement of this manuscript. This research was supported in part by a grant from NASA (NAG5-11007).

## References

- Danjon, A., Recherches sur la photométrie de la lumière cendrée et l'albedo de la terre, *Ann. Obs. Strasbourg*, 2, 165–180, 1928.
- Danjon, A., Albedo, color, and polarization of the Earth, *The Earth as a Planet*, edited by G. P. Kuiper, pp. 726–738, Univ. of Chicago Press, Ill., 1954.
- Dubois, J., Le photomètre à oeil-de-chat et ses applications, *Ciel Terre*, 58, 350–361, 1942.
- Dubois, J., Sur l'albedo de la terre, *Bull. Astron.*, 13, 193–196, 1947.
- Flatte, S., S. E. Koonin, and G. MacDonald, Global change and the dark of the Moon, *Rep. JSR-91-315*, MITRE Corp., McLean, Va., 1991.
- Gibson, G. G., F. M. Denn, D. W. Young, E. F. Harrison, P. Minnis, B. R. Barkstrom, O. C. Smith, and D. J. Travers, Characteristics of the Earth's radiation budget derived from the first year of data from the Earth Radiation Budget Experiment, *SPIE J.*, 1299, 253–256, 1990.
- Goode, P. R., Internal rotation and structure of the Sun, *Rep. ESA SP-376*, pp. 1671–1674, Eur. Space Agency, Paris, 1995.
- Goode, P. R., J. Qiu, V. Yurchyshyn, J. Hickey, M.-C. Chu, E. Kolbe, C. T. Brown, and S. E. Koonin, Earthshine observations of the Earth's reflectance, *Geophys. Res. Lett.*, 28, 1671–1674, 2001.
- Kato, S., N. G. Loeb, and C. K. Rutledge, Estimate of top-of-atmosphere albedo for a molecular atmosphere over ocean using Clouds and the Earth's Radiant Energy System measurements, *J. Geophys. Res.*, 107(D19), 4396, doi:10.1029/2001JD001309, 2002.
- MacDonald, G. J., and S. E. Koonin, Earthshine and climate, *Observ.*, 112, 59–60, 1992.
- Qiu, J., P. R. Goode, E. Pallé, V. Yurchyshyn, J. Hickey, P. Montañés Rodríguez, M.-C. Chu, E. Kolbe, C. T. Brown, and S. E. Koonin, Earthshine and the Earth's albedo: 1. Earthshine observations and measurements of the lunar phase function for accurate measurements of the Earth's Bond albedo, *J. Geophys. Res.*, 108, doi:10.1029/2003JD003610, in press, 2003.
- Rossov, W. B., A. W. Walker, D. E. Beuschel, and M. D. Roiter, International Satellite Cloud Climatology Project (ISCCP): Documentation of new cloud datasets, *Rep. WMO/TD-No. 737*, 115 pp., World Meteorol. Organ., Geneva, Switzerland, 1996.
- Suttles, J. T., R. N. Green, P. Minnis, G. L. Smith, W. G. Staylor, B. A. Wielicki, I. J. Walker, V. R. Young, and L. L. Stowe, *Angular Radiation Models for Earth-Atmosphere Systems*, vol. 1, *Shortwave Radiation, Ref. Publ. RP-1184*, 26 pp., NASA, Hampton, Va., 1988.
- C. T. Brown and S. E. Koonin, W. K. Kellogg Radiation Laboratory, California Institute of Technology, 206 Parsons-Gates, Pasadena, CA 91125, USA. (titus@caltech.edu; koonin@caltech.edu)
- M.-C. Chu, Department of Physics, The Chinese University of Hong Kong, Room 108, 1st floor, Science Center (North Block), Shatin N. T., Hong Kong, China. (mcchu@phy.cuhk.hk)
- P. R. Goode, J. Hickey, E. Pallé, J. Qiu, P. Montañés Rodríguez, and V. Yurchyshyn, Big Bear Solar Observatory, New Jersey Institute of Technology, Newark, NJ 07102, USA. (pgoode@bbso.njit.edu; jhickey@astro.caltech.edu; epb@bbso.njit.edu; qiu@bbso.njit.edu; pmr@bbso.njit.edu; vayur@bbso.njit.edu)
- E. Kolbe, Department für Physik und Astronomie, Universität Basel, Klingelbergstrasse 82, 4056 Basel, Switzerland. (kolbe@quasar.physik.unibas.ch)